

<sup>1</sup> Defocus Corrected Large Area Cryo-EM (DeCo-LACE) for Label-Free  
<sup>2</sup> Detection of Molecules across Entire Cell Sections

<sup>3</sup>

<sup>4</sup> This manuscript (permalink) was automatically generated from jojoelfe/deco\_lace\_template\_matching\_manuscript@9f26f34  
<sup>5</sup> on May 20, 2022.

<sup>6</sup> **Authors**

- <sup>7</sup> • **Johannes Elferich**  0000-0002-9911-706X ·  jojoelfe RNA Therapeutic Institute, UMass Chan Medical  
<sup>8</sup> School; HHMI
- <sup>9</sup> • **Nikolaus Grigorieff**  0000-0002-1506-909X ·  nikogrigorieff RNA Therapeutic Institute, UMass Chan  
<sup>10</sup> Medical School; HHMI

<sup>11</sup> **Abstract**

<sup>12</sup> Localization of biomolecules inside a cell is an important goal of biological imaging. Fluorescence microscopy  
<sup>13</sup> can localize biomolecules inside whole cells and tissues, but its ability to count biomolecules and accuracy of the  
<sup>14</sup> spatial coordinates is limited by the wavelength of visible light. Cryo-electron microscopy (cryo-EM) provides highly  
<sup>15</sup> accurate position and orientation information of biomolecules but is often confined to small fields of view inside  
<sup>16</sup> a cell, limiting biological context. In this study we use a new data-acquisition scheme called “Defocus-Corrected  
<sup>17</sup> Large-Area cryo-EM” (DeCo-LACE) to collect high-resolution cryo-EM data over entire sections (100 – 200 nm  
<sup>18</sup> thick lamellae) of neutrophil-like mouse cells, representing 1-2% of the total cellular volume. We use 2D template  
<sup>19</sup> matching (2DTM) to determine localization and orientation of the large ribosomal subunit in these sections. These  
<sup>20</sup> data provide “maps” of translational activity across sections of mammalian cells. This new high-throughput cryo-  
<sup>21</sup> EM data collection approach together with 2DTM will advance visual proteomics and complement other single-cell  
<sup>22</sup> “omics” techniques, such as flow-cytometry and single-cell sequencing.

<sup>23</sup> **Introduction**

<sup>24</sup> A major goal in understanding cellular processes is the knowledge of the amounts, location, interactions, and  
<sup>25</sup> conformations of biomolecules inside the cell. This knowledge can be obtained by approaches broadly divided into  
<sup>26</sup> label- and label-free techniques. In label-dependent techniques a probe is physically attached to a molecule of  
<sup>27</sup> interest that is able to be detected by its strong signal, such as a fluorescent molecule. In label-free techniques,  
<sup>28</sup> the physical properties of molecules themselves are used for detection. An example for this is proteomics using  
<sup>29</sup> mass-spectrometry [1]. The advantage of label-free techniques is that they can provide information over thousands  
<sup>30</sup> of molecules, while label-dependent techniques offer highly specific information for a few molecules. Especially  
<sup>31</sup> spatial information can often only be achieved using label-dependent techniques, such as fluorescence microscopy  
<sup>32</sup> [2].

<sup>33</sup> Cryo-electron microscopy (cryo-EM) has the potential to directly visualize the arrangement of atoms that compose  
<sup>34</sup> biomolecules inside of cells, thereby allowing label-free detection with high spatial accuracy. This has been called  
<sup>35</sup> “visual proteomics” [3]. Since cryo-EM requires thin samples (<500nm), imaging of biomolecules inside cells is  
<sup>36</sup> restricted to small organisms, thin regions of cells, or samples that have been suitably thinned. Thinning can  
<sup>37</sup> be achieved either by mechanical sectioning [4] or by milling using a focused ion beam (FIB) [5]. This complex  
<sup>38</sup> workflow leads to a low throughput of cryo-EM imaging of cells and is further limited by the fact that at the required  
<sup>39</sup> magnifications, typical fields of view (FOV) are very small compared to mammalian cells, and the FOV achieved  
<sup>40</sup> by label-dependent techniques such as fluorescence light microscopy. The predominant cryo-EM technique for  
<sup>41</sup> the localization of biomolecules of defined size and shape inside cells is cryo-electron tomography [6]. However, the  
<sup>42</sup> requirement of a tilt series at every imaged location and subsequent image alignment, severely limits the throughput  
<sup>43</sup> for molecular localization.

<sup>44</sup> An alternative approach is to identify molecules by their structural “fingerprint” in single projection using “2D  
<sup>45</sup> template-matching” (2DTM) [7,8,9]. In this method, a 3D model of a biomolecule is used as a template to find 2D  
<sup>46</sup> projections that match the molecules visible in the electron micrographs. This method requires a projection search  
<sup>47</sup> on a fine angular grid, and the projections are used to find local cross-correlation peaks with the micrograph. Since  
<sup>48</sup> the location of a biomolecule in the z-direction causes predictable aberrations to the projection image, this method  
<sup>49</sup> can be used to calculate complete 3D coordinates and orientations of a biomolecule in a cellular sample [8].

<sup>50</sup> Here we apply 2DTM of the ribosome large subunit (LSU) to cryo-FIB milled neutrophil-like murine cells [10].  
<sup>51</sup> We chose these cells because genetic defects in the ribosome machinery often leads to hematopoietic disease [11]  
<sup>52</sup> and direct quantification of ribosome location, number and conformational states in hematopoietic cells could lead  
<sup>53</sup> to new insight into hematopoietic disease [12]. To increase the amount of collected data and to provide unbiased  
<sup>54</sup> sampling of the whole lamella, we devised a new data-acquisition scheme, “Defocus-Corrected Large Area Cryo-  
<sup>55</sup> Electron microscopy” (DeCo-LACE). 2DTM allows us to test whether aberrations caused by large beam-image

shifts and highly condensed beams deteriorate the high-resolution signal. We find that these aberrations do not impede LSU detection by 2DTM. The resulting data provide a description of ribosome distribution in an entire lamella, which represent 1-2% of the cellular volume. We find a highly heterogeneous density of ribosomes within the cell. Analysis of the throughput in this method suggests that for the foreseeable future computation will be the bottleneck for visual proteomics.

## Materials and Methods

### Grid preparation

ER-HoxA9 cells were maintained in RPMI medium supplemented with 10% FBS, penicillin/streptomycin, SCF, and estrogen [10] at 37 °C and 5% CO<sub>2</sub>. 120 h prior to grid preparation, cells were washed twice in PBS and cultured in the same medium except without estrogen. Differentiation was verified by staining with Hoechst-dye and inspection of nuclear morphology. Cells were then counted and diluted to 1 · 10<sup>6</sup> cells/ml. Grids (either 200 mesh copper grids, with a silicone-oxide and 2 µm holes with a 2 µm spacing or 200 mesh gold grids with a thin gold film and 2 µm holes in 2 µm spacing) were glow-discharged from both sides using a 15 mA for 45 s. 3.5 µl of cell suspension was added to grids on the thin-film side and grids were blotted from the back side using a GP2 cryoplunger (Leica) for 8 s and rapidly plunged into liquid ethane at -185 °C.

### FIB-milling

Grids were loaded into an Aquilos 2 FIB/SEM (Thermo Fisher) instrument with a stage cooled to -190 °C. Grids were sputter-coated with platinum for 15 s at 45 mA and then coated with a layer of platinum-precursor by opening the GIS-valve for 45 s. An overview of the grid was created by montaging SEM images and isolated cells at the center of gridsquares were selected for FIB-milling. Lamellae were generated automatically using the AutoTEM software (Thermo Fisher), with the following parameters:

- Milling angle: 20°
- Rough milling: 3.2 µm thickness, 0.5 nA current
- Medium milling: 1.8 µm thickness, 0.3 nA current, 1.0° overtilt
- Fine milling: 1.0 µm thickness, 0.1 nA current, 0.5° overtilt
- Finer milling: 700 nm thickness, 0.1 nA current, 0.2° overtilt
- Polish 1: 450 nm thickness, 50 pA current
- Polish 2: 200 nm thickness, 30 pA current

This resulted in 6-10 µm wide lamella with 150-250 nm thickness as determined by FIB-imaging of the lamella edges.

86 **Data collection**

87 Grids were loaded into a Titan Krios TEM (Thermo Fisher) operated at 300 keV and equipped with a BioQuantum  
88 energy filter (Gatan) and K3 camera (Gatan). The microscope was aligned using a cross-grating grid on the stage.  
89 Prior to each session, we carefully performed the “Image/Beam” calibration in nanoprobe. We set the magnification  
90 to a pixel size of 1.76 Å and condensed the beam to ~ 900 nm diameter, resulting in the beam being completely  
91 visible on the camera. To establish fringe-free conditions, the “Fine eucentric” procedure of SerialEM [13] was used  
92 to move a square of the cross-grating grid to the eucentric position of the microscope. The effective defocus was  
93 then set to 2 µm, using the “autofocus” routine of SerialEM. The objective focus of the microscope was changed  
94 until no fringes were visible. The stage was then moved in Z until images had an apparent defocus of 2 µm. The  
95 difference in stage Z-position between the eucentric and fringe-free conditions was used to move other areas into  
96 fringe-free condition.

97 Low magnification montages were used to find lamellae and lamellae that were sufficiently thin and free of con-  
98 tamination were selected for automated data collection. Overview images of each lamella were taken at 2250x  
99 magnification (38 Å pixel size). The corners of the lamella in the overview image were manually annotated in  
100 SerialEM and translated into beam image-shift values using SerialEM’s calibration. A hexagonal pattern of beam  
101 image-shift positions was calculated that covered the area between the four corners in a serpentine way, with a 30  
102  $\sqrt{3} \cdot 425$  nm horizontal spacing and  $3/4 \cdot 850$  nm vertical spacing. Exposures were taken at each position with a 30  
103  $e^-/\text{\AA}^2$  total dose. After each exposure, the defocus was estimated using the ctffind function of SerialEM and the  
104 focus for the next exposure was corrected by the difference between the estimated focus and the desired defocus of  
105 800 nm. Furthermore, after each exposure the deviation of the beam from the center of the camera was measured  
106 and corrected using the “CenterBeamFromImage” command of SerialEM.

107 After data collection, a 20 s exposure at 2250x magnification of the lamella at 200 m defocus was taken for  
108 visualization purposes. A Python script implementing this procedure is available at [Link to repo].

109 **DeCo-LACE data processing**

110 An overview of the data analysis pipeline is shown in Fig. 1.

111 **Pre-processing** Motion-correction, dose weighting and other preprocessing as detailed below was performed  
112 using *cisTEM* [14]. To avoid influence of the beam-edge on motion-correction, only a quarter of the movie in the  
113 center of the camera was considered for calculation of the estimated motion. After movie frames were aligned and  
114 summed, a mask for the illuminated area was calculated by lowpass filtering the image with a 100 Å resolution  
115 cutoff, thresholding the image at 10% of the maximal value and then lowpass filtering the mask again with a 100 Å  
116 resolution cutoff to smooth the mask edges. This mask was then used to select dark areas in the image and fill the

117 pixels with Gaussian noise, with the same mean and standard deviation as the illuminated area. A custom version  
 118 of the unblur program [15] implementing this procedure is available at [link to decolace branch]. During motion  
 119 correction images were resampled to a pixel size of 1.5 Å. The contrast-transfer function (CTF) was estimated using  
 120 ctffind [16], searching between 0.2 and 2 m defocus.

121 **2DTM** The search template was generated from the atomic model of the mouse LSU (PDB 6SWA, exluding the  
 122 Epb1 subunit) using the cryo-EM simulator implemented in *cisTEM* [17]. The match\_template program [9] was  
 123 used to search for this template in the movie-aligned, exposure-filtered and masked images, using a 1.5° angular  
 124 step in out-of-plane angles and a 1.0° angular step in-plane. 11 defocus planes in 20 nm steps centered around the  
 125 ctffind-determined defocus were searched. Targets were defined as detected when their matches with the template  
 126 produced peaks with a singal-to-noise ratio (SNR) above a threshold of 7.75, which was chosen based on the  
 127 one-false-positive-per-tile criterion [7].

128 **Montage assembly** The coordinates of each tile  $i$ ,  $\mathbf{c}_i$  [2D Vector in pixels] were initialized using beam image-shift  
 129 of the tile,  $\mathbf{b}_i$  [2D Vector in m], and the ISToCamera matrix  $\mathbf{IC}$ , as calibrated by SerialEM:

$$\mathbf{c}_i = \mathbf{IC} \cdot \mathbf{b}_i$$

130 A list of tile pairs  $i, j$  that overlap were assembled by selecting images where  $|\mathbf{c}_i - \mathbf{c}_j| < D_{Beam}$ . In order to calculate  
 131 the precise offset between tiles  $i$  and  $j$ ,  $\mathbf{r}_{i,j}$ , we calculated the cross-correlation between the two tiles, masked to  
 132 the overlapping illuminated area using the scikit-image package [18] was used to calculate refined offsets . The  
 133 coordinates  $\mathbf{c}_i$  were then refined by a least-square minimization against  $\mathbf{r}_{i,j}$ :

$$\min_{\mathbf{c}} \sum_{pairs} (\mathbf{r}_{i,j} - (\mathbf{c}_i - \mathbf{c}_j))^2$$

134 using the scipy package [19]. The masked cross-correlation and the least-square minimization was repeated once  
 135 more to arrive at the final tile alignment.

136 The x,y coordinates of target  $n$  detected by 2DTM in the tile  $i$ ,  $\mathbf{m}_{n,i}^T$ , was transformed into the montage frame by  
 137 adding the coordinate of the tile.

$$\mathbf{m}_n^M = \mathbf{m}_{n,i}^T + \mathbf{c}_i$$

138 The z coordinate of each target was calculated as the sum of the defocus offset for the target, the estimated defocus  
 139 of the tile, and the nominal defocus of the microscope when the tile was acquired.

<sup>140</sup> Images were rendered using UCSF ChimeraX [20]. The Python scripts used for data processing are available under  
<sup>141</sup> [repolink].

## <sup>142</sup> Results

### <sup>143</sup> 2DTM detects large ribosomal subunits in cryo-FIB lamellae of mammalian cells

<sup>144</sup> To test whether we could detect individual ribosomes in mammalian cells we prepared cryo-lamellae of mouse  
<sup>145</sup> neutrophil-like cells. An overview image of a representative lamella clearly shows cellular features consistent with  
<sup>146</sup> a neutrophil-like phenotype, mainly a segmented nucleus and a plethora of membrane-organelles, corresponding to  
<sup>147</sup> the granules and secretory vesicles of neutrophils (Fig. [2]A). We then proceeded to acquire micrographs on this  
<sup>148</sup> lamella with a defocus of 0.5-1.0 m, 30 e<sup>-</sup>/Å<sup>2</sup>/s exposure and 1.76 Å pixel size. We manually selected multiple  
<sup>149</sup> locations in the lamella and acquired micrographs using standard low-dose techniques where focusing is performed  
<sup>150</sup> on a sacrificial area. The resulting micrographs showed smooth bilayered membranes and no signs of crystalline ice  
<sup>151</sup> (Fig. [2]C,D), indicating successful vitrification throughout the lamella. Successful vitrification is facilitated by the  
<sup>152</sup> small size (~8 m diameter) of these cells.

<sup>153</sup> We used an atomic model of the 60S mouse ribosomal subunit (6SWA) for 2DTM [21]. In a subset of images,  
<sup>154</sup> the distribution of cross-correlation scores significantly exceeded the distribution expected from images devoid of  
<sup>155</sup> detectable targets. In the resulting scaled maximum-intensity projections (MIPs), clear peaks with SNR values up  
<sup>156</sup> to 10 were apparent (Fig. [2 - figure supplement 1]A). Using a threshold criterion to select significant targets (see  
<sup>157</sup> Methods), we found that in images of cytosolic compartments there were 10-500 ribosomes within one micrograph  
<sup>158</sup> (Fig. [2]B-E). Notably, we found no targets in areas corresponding to the nucleus (Fig. [2]B) or mitochondria  
<sup>159</sup> (Fig. 1D). In the cytoplasm, we found a highly variable number of targets, only ~ 50 in some exposures (Fig. [2]E)  
<sup>160</sup> and up to 500 in others (Fig. [2]C). This is a ten-fold difference in local ribosome concentration, highlighting the  
<sup>161</sup> importance of imaging larger areas of a lamella to gain a complete picture of target distributions. We therefore set  
<sup>162</sup> out to collect cryo-EM data for 2DTM from mammalian cell lamellae in a high-throughput unbiased fashion.

### <sup>163</sup> DeCo-LACE for 2D imaging of whole lamellae

<sup>164</sup> In order to obtain high-resolution data from complete lamellae, we used a new approach for data collection. This  
<sup>165</sup> approach uses three key strategies: (1) every electron that exposes a fresh area of the sample is collected on the  
<sup>166</sup> camera (2) image shift is used to precisely and quickly raster the surface of a lamella and (3) focusing is done  
<sup>167</sup> without using a sacrificial area (Fig. [3]A).

<sup>168</sup> To ensure that every electron exposing a fresh area of the sample is captured by the detector, we adjusted the  
<sup>169</sup> electron beam size to be entirely contained by the detector area. During canonical low-dose imaging, the microscope  
<sup>170</sup> is configured so that the focal plane is identical to the eucentric plane of the specimen stage. This leaves the C2

171 aperture out of focus, resulting in ripples at the edge of the beam (Fig. [3]D). While these ripples are low-resolution  
172 features that likely do not interfere with 2DTM [cite], we also tested data collection under conditions where the C2  
173 aperture is in focus (“fringe-free”, Fig. [3]E).

174 We then centered a lamella on the optical axis of the microscope and used the image shift controls of the microscope  
175 to systematically scan the whole surface of the lamella in a hexagonal pattern (Fig. [3]A,C). Instead of focusing  
176 on a sacrificial area, we determined the defocus from every exposure after it was taken. The defocus was then  
177 adjusted based on the difference between desired and measured defocus (Fig. [3]B). Since we used a serpentine  
178 pattern for data collection, every exposure was close to the previous exposure, making large changes in the defocus  
179 unlikely. Furthermore, we started our acquisition pattern on the platinum deposition edge to make sure that the  
180 initial exposure where the defocus was not yet adjusted did not contain any biologically relevant information.

181 We used this strategy to collect data on eight lamellae, four using the eucentric focus condition, hereafter referred to  
182 as Lamella<sub>EUC</sub>, and four using the fringe-free condition, hereafter referred to as Lamella<sub>FFF</sub>(Fig. [4] A+D, Fig. [4]  
183 - figure supplement 4]A). We were able to collect data with a highly consistent defocus of 800 nm (Fig. [3]F), both  
184 in the eucentric focus and fringe-free focus condition. To ensure that data were collected consistently, we mapped  
185 defocus values as a function of the applied image shift (Fig. [3 - figure supplement 1]A). This demonstrated that  
186 the defocus was consistent across a lamella, except for rare outliers and in images containing contamination. We  
187 also plotted the measured objective astigmatism of each lamella and found that it varies with the applied image  
188 shift, becoming more astigmatic mostly due to image shift in the x direction (Fig. [3 - figure supplement 1]B).  
189 While approaches exist to correct for this during the data collection [22], we opted to not use these approaches in  
190 our initial experiments. We reasoned that because 2DTM depends on high-resolution information, this would be  
191 an excellent test of how much these aberration affect imaging.

192 We assembled the tile micrographs into a montage using the image-shift values and the SerialEM calibration followed  
193 by cross-correlation based refinement (see Methods). In the resulting montages, the same cellular features visible  
194 in the overview images are apparent (Fig. [4]B+E, Fig. [4 - figure supplement 4]B), however due to the high  
195 magnification and low defocus many more details, such as the membrane bilayer separation, can be observed (Fig.  
196 [4]C+F). For montages collected using the eucentric condition, there are clearly visible fringes at the edges between  
197 the tiles (Fig. [4]C), which are absent in the fringe-free focus montages (Fig. [4]F). In our analysis below, we show  
198 that these fringes do not impede target detection by 2DTM, making them primarily an aesthetic issue. We also  
199 note that the tiling pattern is visible in the montages (Fig. [4]B+E), which we believe is due to the non-linear  
200 behavior of the K3 camera since we can observe these shading artifacts in micrographs of a condensed beam over  
201 vacuum (Fig. [4 - figure supplement 3]).

202 The montages show membrane vesicles and granules with highly variable sizes and density. We found that a  
203 substantial number of granules, which are characterized by higher density inside the the surrounding cytosol [23],

204 seemed to contain a membrane-enclosed inclusion with density similar to the surrounding cytosol (Fig. [4 - figure  
205 supplement 4]C) and could therefore be formed by an autophagy-like pathway. These granules were 150-300 nm  
206 in diameter and the inclusions were 100-200 nm in diameter. Based on these dimensions the granules are either  
207 azurophil or specific granules [23]. To our knowledge, these inclusion have not been described in granulocytes and  
208 are further described and discussed below.

## 209 **2DTM of DeCo-LACE data reveals ribosome distribution in cellular cross-sections**

210 In our initial attempts of using 2DTM on micrographs acquired with the DeCo-LACE protocol, we did not observe  
211 any SNR peaks above threshold using the large subunit of the mouse ribosome (Fig. [4 - figure supplement 1]A).  
212 We reasoned that the edges of the beam might interfere with motion-correction of the movies as they represent  
213 strong low-resolution features that do not move with the sample. When we cropped the movie frames to exclude the  
214 beam edges, the estimated amount of motion increased (Fig. [4 - figure supplement 1]B), consistent with successful  
215 tracking of sample motion. Furthermore, in the motion-corrected average we could identify significant SNR peaks  
216 (Fig. [4 - figure supplement 1]B), confirming to high sensitivity of 2DTM to the presents of high-resolution signal  
217 preserved in the images by the motion correction. To streamline data processing, we implemented a function in  
218 unblur to consider only a defined central area of a movie for estimation of sample motion, while still averaging the  
219 complete movie frames (Fig. [4 - figure supplement 1]C). Using this approach, we motion-corrected all tiles in the  
220 eight lamellae and found consistently total motion below 1 Å per frame (Fig. [4 - figure supplement 2] A). In some  
221 lamellae we found increased motion in the lamella center, which indicates areas of variable mechanical stability  
222 within FIB-milled lamellae. In some micrographs we also observed that the beam edges gave rise to artifacts in  
223 the MIP and numerous false-positive detections at the edge of the illuminated area (Fig. [4 - figure supplement  
224 1]D). A similar phenomenon was observed on isolated “hot” pixels in unilluminated areas. To overcome this issue  
225 we implemented a function in unblur to replace dark areas in the micrograph with Gaussian noise (see Methods),  
226 with mean and standard deviation matching the illuminated portion of the micrograph (Fig. [4 - figure supplement  
227 1]D+E). Together, these pre-processing steps enabled us to perform 2DTM on all tiles of the eight lamellae.

228 We used the refined tile positions to calculate the positions of the detected LSUs in the lamellae (Fig. [6]A, Fig. [7]A).  
229 Overlaying these positions of the lamellae montages reveal ribosome distribution throughout the FIB-milled slices  
230 of individual cells. Organelles like the nucleus and mitochondria only showed sporadic targets detected with low  
231 SNRs, consistent with the estimated false-positive rate of one per tile. For each detected target we also calculated  
232 the Z positions from the individual estimated defocus and defocus offset for each tile. When viewed from the side,  
233 the ribosome positions therefore show the slight tilts of the lamellae relative to the microscope frame of reference  
234 (Fig. [6]B, Fig. [7]B). Furthermore, the side views indicated that lamellae were thinner at the leading edge. Indeed,  
235 when plotting the transmitted beam intensities in individual tiles as a function of beam image-shift, we observed  
236 substantially higher intensities at the leading edge (Fig. [4 - figure supplement 2]B), which in energy-filtered TEM

237 indicates a thinner sample [24]. Even though we prepared the lamellae with the “overtilt” approach [25], this means  
238 that ribosome densities across the lamellae can be skewed by a change in thickness, and better sample preparation  
239 methods are needed to generate more even samples.

240 Close inspection of the ribosome positions in the lamellae revealed several interesting features. Ribosomes could  
241 be seen associating with membranes, in patterns reminiscent of the rough endoplasmic reticulum (Fig. [6]C, Fig.  
242 [7]C) or the outer nuclear membrane (Fig. [6]D). We also observed ribosomes forming ring-like structures (Fig.  
243 [6]E), potentially indicating circularized mRNAs [26]. While ribosomes were for the most part excluded from the  
244 numerous granules observed in the cytoplasm, in some cases we observed clusters of ribosomes in the inclusions of  
245 double-membraned granules described earlier (Fig. [6]F, Fig. [7]D,E). It is, in principle, possible that these targets  
246 are situated above or below the imaged granules, since the granule positions in z cannot be determined using 2D  
247 projections. However, in the case of Fig. [7]E, the detected ribosomes span the whole lamella in the z direction  
248 (Fig. [7]F), while positions above or below a granule would result in ribosomes situated exclusively at the top or  
249 bottom of the lamella. This conclusive evidence of ribosomes in inclusions is consistent with the earlier hypothesis  
250 that the inclusions are of cytoplasmic origin.

## 251 Does DeCo-LACE induce aberrations that affect 2DTM?

252 Within the eight lamellae we found different number of detected targets (Fig. [5]A). Lamella<sub>EUC</sub> 1 had the most  
253 detected targets, but also has the largest surface area and contained cytoplasm from two cells. Lamella<sub>FFF</sub> 4 had  
254 the fewest detected targets, but this particular lamella was dominated by a circular section of the nucleus, with only  
255 small pockets of cytoplasm (Fig. [4 - figure supplement 4]). In an attempt to normalize for these differences in area  
256 containing cytoplasm, we compared the number of detected targets per tile in tiles that contained more than one  
257 target, which should exclude tiles with non-cytosolic content (Fig. [5]B). While this measure had less variability,  
258 there were still differences. Lamella<sub>EUC</sub> 4 had not only the fewest targets, but also the lowest density, which could  
259 be due to this lamella being the thinnest, or due to it sectioning the cell in an area with a lower concentration of  
260 ribosomes. Lamella<sub>FFF</sub> 3 had a substantially higher number of ribosomes per tile. Since all of these lamellae were  
261 made from a cell-line under identical conditions, this underscores the necessity to collect data from large numbers  
262 of lamellae to overcome the inherent variability. When comparing the distribution of scores between lamellae, we  
263 found them to be fairly comparable with median SNRs ranging from 8.7 to 9.7 (Fig. [5]C). Lamella<sub>EUC</sub> 1 had  
264 slightly lower scores compared to the rest, potentially due to its large size and connected mechanical instability  
265 during imaging. Overall, we did not observe differences in the number or SNR of detected targets between eucentric  
266 or fringe-free illumination conditions that were bigger than the observed inter-lamella variability.

267 Since the SNR values of 2DTM are highly sensitive to image quality, we reasoned we could use them to verify  
268 that DeCo-LACE does not introduce a systematic loss of image quality. We considered non-parallel illumination

269 introduced by the unusually condensed beam and uncharacterized aberrations near the beam periphery. When  
270 plotting the SNR values of detected targets in all eight lamellae as a function of their location in the tiles, we found  
271 uniformly high SNR values throughout the illuminated areas for both eucentric and fringe-free focus illumination,  
272 demonstrating that both illumination schemes are suitable for DeCo-LACE (Fig. [5]D).

273 We also wondered whether large image shifts would lead aberration due to astigmatism or beam tilt [22]. We  
274 reasoned that if that was the case the number of detected targets should be highest in the center of the lamella  
275 where the applied beam image-shift is 0. Instead we observed that in both eucentric and fringe-free focus conditions  
276 more targets were detected at the “back” edge of the lamella (Fig. [5]E). This may be due to the center of the  
277 cell being predominantly occupied by the nucleus, despite its segmentation in neutrophil-like cells. The increase in  
278 matches at the “back” of the lamellae compared to the “front” can also be explained by the thickness gradient of the  
279 lamellae (Fig. [4 - figure supplement 2]B, Fig. [6]B, Fig. [7]B). In addition, aberrations would be expected to cause  
280 average 2DTM SNRs to be higher when beam-image shift values are small. Instead, we found that SNRs were  
281 on average the highest at the “front” edge of the lamellae, presumably due to the thinner sample. We therefore  
282 conclude that factors other than beam image-shift or beam condensation aberrations are limiting 2DTM SNRs,  
283 predominantly the thickness of the lamellae.

#### 284 Computation is the bottleneck of visual proteomics

285 As described above, the variability of lamellae, both in terms of experimental parameters including area, thickness  
286 and mechanical stability, and in terms of biology, such as selection of cell type and location of the section within the  
287 cell, requires collection of orders of magnitude more data than in this study to draw quantitative and statistically  
288 relevant conclusions about the number and location of molecules under different experimental conditions. The  
289 samples used were prepared in two 24 h sessions on a FIB/SEM instrument, and imaging was performed during  
290 another two 24h session on the TEM microscope. Inspections of the timestamps of the raw data files revealed that  
291 the milling time per lamella was ~30 minutes and TEM imaging was accomplished in ~10 seconds per tile or 90  
292 minutes for a ~ 6x6 m lamella. Processing of the data, however, took substantially longer. Specifically, 2DTM of  
293 all tiles took approximately one week per lamella on 32 A100 GPUs. Computation is therefore a bottleneck in our  
294 current workflow, and further optimizations of the algorithm may be necessary to increase throughput. Alternatively,  
295 this bottleneck could be reduced by increasing the number of processing units.

#### 296 Discussion

297 In this study we developed an approach to image entire cellular cross-section using cryo-EM at high enough resolution  
298 to allow for 2DTM detection of the LSU. The two main advantages compared to previous approaches are a high  
299 throughput of imaging and the biological context for detected molecules. The requirement to increase throughput in  
300 cryo-EM data collection of cellular samples has been recognized in the recent literature. Most approaches described

301 so far are tailored towards tomography. Peck et al. [27] and Yang et al. [28] developed approaches to increase the  
302 FOV of tomogram data-collection by using a montaging technique. Peck et al. used a similar “condensed-beam”  
303 approach as described here. However, the montages are substantially smaller in scope, covering carbon film holes  
304 of 2 um diameter. Bouvette et al. [29] and Eisenstein et al. [30] are using beam image-shift to collect tilt-series in  
305 multiple locations in parallel to increase throughput. However, none of these approaches provide the full coverage  
306 of a cellular cross-section that can be achieved using DeCo-Lace.

307 Since we observed substantial variation in ribosome density within and between lamellae, visual proteomics studies  
308 that use cryo-EM to establish changes in molecular organization within cells will require orders of magnitude more  
309 data than used in this study. One milestone would be to image enough data to represent one cellular volume, which  
310 for a small eukaryotic cells requires imaging approximately 100 lamella. While data collection throughput on the  
311 TEM is fundamentally limited by the exposure time, this amount of data could be collected within 12 hour by  
312 improving the data acquisition scheme to perform all necessary calculation in parallel with actual exposure of the  
313 camera. Sample preparation using a FIB/SEM is also currently a bottleneck, but preparation of large lamellae with  
314 multiple cellular cross-sections using methods like WAFFLE [31] might allow sufficient throughput. As stated in  
315 the results, at least for 2DTM computation will remain challenging and approximately 17,000 GPU hours would  
316 be required for a 100 lamellae dataset.

317 As described in [7] the 2DTM SNR threshold for detecting a target is chosen to result in one false positive detection  
318 per image searched. We would therefore expect to find one false positive detection per tile. We reasoned that the  
319 large nuclear area imaged by DeCo-Lace could be used to test whether this assumption is true. In the 670 tiles  
320 containing exclusively nucleus (as manually annotated from the overview image) we detected 247 targets, making  
321 the false-positive rate more than twofold lower than expected. Since earlier work shows that 2DTM with the LSU  
322 can produce matches to nuclear ribosome biogenesis intermediates [32], this could even be an overestimate of the  
323 false-positive rate. This suggests that the detection threshold could be even lower, which is an area of ongoing  
324 research.

325 We found that even though we used beam image-shift extensively (up to 7 um), we did not see substantially reduced  
326 2DTM SNR values in tiles acquired at high beam image-shift compared to tiles acquired with low or no beam image-  
327 shift. This is in contrast to reports in single-particle analysis (SPA) [33] where the induced beam tilt substantially  
328 reduced the resolution if it was not corrected during processing. It is possible that 2DTM is less sensitive to beam-  
329 tilt aberrations, since the template is free of any aberration and only the image is distorted, while in SPA the beam  
330 tilt will affect both the images and the reconstructed template.

331 As mentioned in the results, we found a consistent shading artifact pattern in our montages, that we believe is the  
332 result of non-linear behavior of the K3 camera. Indeed, when we average images with a condensed beam taken  
333 over vacuum we found in both focus conditions a consistent background pattern with a brighter region on the

334 periphery of the illuminated area (Fig [4 - figure supplement 3]). This might be caused by dynamic adjustment  
335 of the internal camera counting threshold which expects columns of the sensor to be evenly illuminated as is the  
336 case for SPA applications. Since the signal of this pattern has mainly low-resolution components it is unlikely to  
337 affect 2DTM. However, it highlights that the non-linear behavior of the camera has to be taken into account when  
338 imaging samples with strongly varying density and unusual illumination schemes.

339 Unexpectedly, we observed granules containing a vesicle of putative cytosolic origin. We speculate that upon  
340 degranulation, the process in which granules fuse with the plasma membrane, these vesicles would be released  
341 into the extracellular space. The main types of extracellular vesicles of this size are exosomes, up to 100 nm  
342 large vesicles derived from fusion of multivesicular bodies with the plasma membrane, and microvesicles, which are  
343 derived from direct budding of the plasma membrane [34]. We suggest that granulocytes could release a third type  
344 of extracellular vesicle, granule-derived vesicles (GDV), into the extracellular space. 2DTM showed that a subset  
345 of GDVs can contain ribosomes (Fig. [6]F, Fig. [7]D,E). This could indicate that these vesicles are transporting  
346 translation-capable mRNAs, as has been described for exosomes [35]. Further studies will be necessary to confirm  
347 the existence of GDVs in granulocytes isolated from mammals and to understand their functional significance.

## 348 Figures

## 349 References

- 350 1. **Label-free, normalized quantification of complex mass spectrometry data for proteomic analysis** Noelle M Griffin, Jingyi Yu, Fred Long, Phil Oh, Sabrina Shore, Yan Li, Jim A Koziol, Jan E Schnitzer  
*Nature Biotechnology* (2010-01) <https://doi.org/fshgnc> DOI: 10.1038/nbt.1592 · PMID: 20010810 · PMCID: PMC2805705
- 351 2. **Fluorescence microscopy** Jeff W Lichtman, José-Angel Conchello  
*Nature Methods* (2005-11-18) <https://doi.org/bbpg4n> DOI: 10.1038/nmeth817 · PMID: 16299476
- 353 3. **A visual approach to proteomics** Stephan Nickell, Christine Kofler, Andrew P Leis, Wolfgang Baumeister  
*Nature Reviews Molecular Cell Biology* (2006-02-15) <https://doi.org/d6d5mq> DOI: 10.1038/nrm1861 · PMID: 16482091

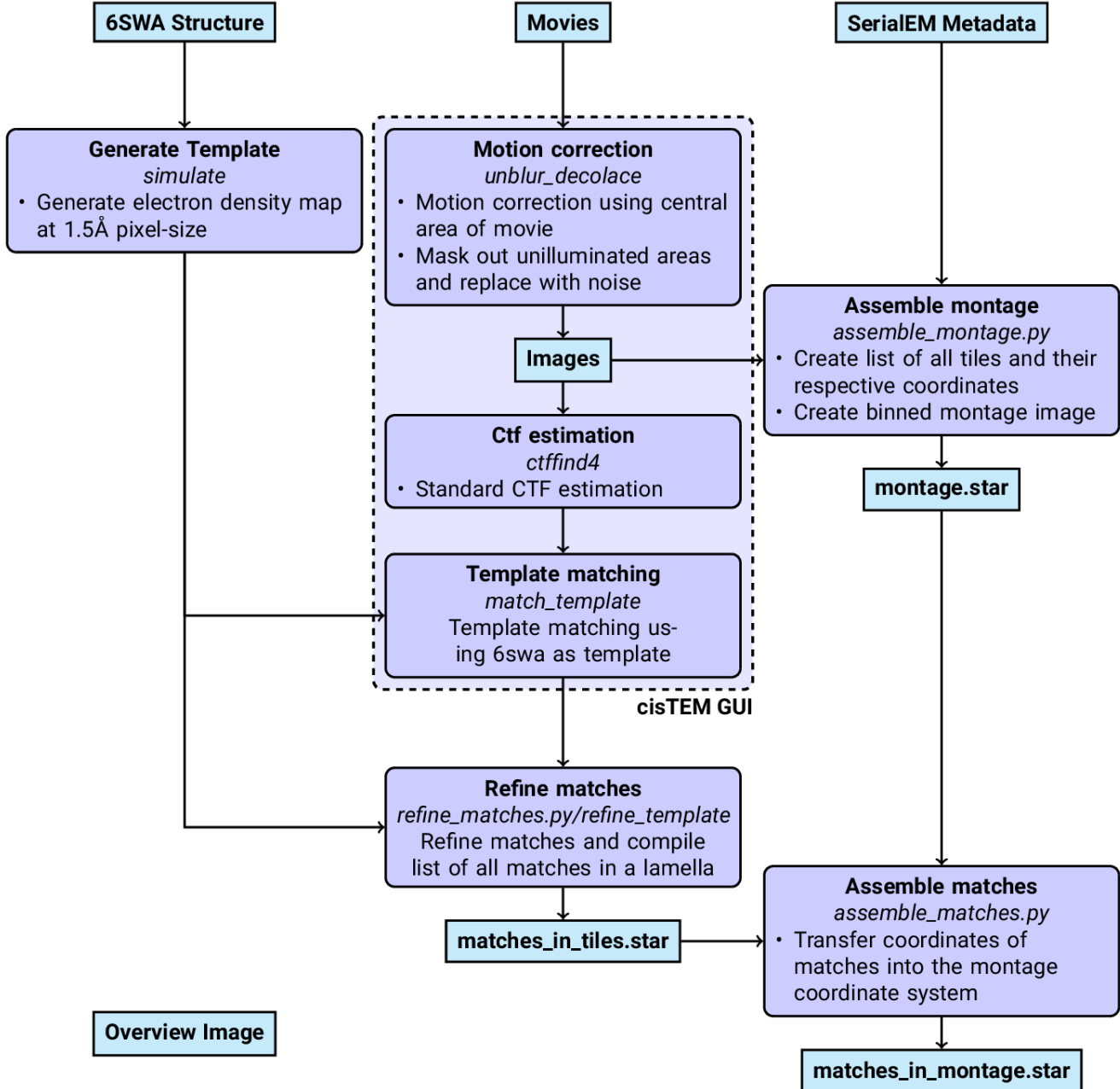


Figure 1: Workflow of DeCo-Lace processing

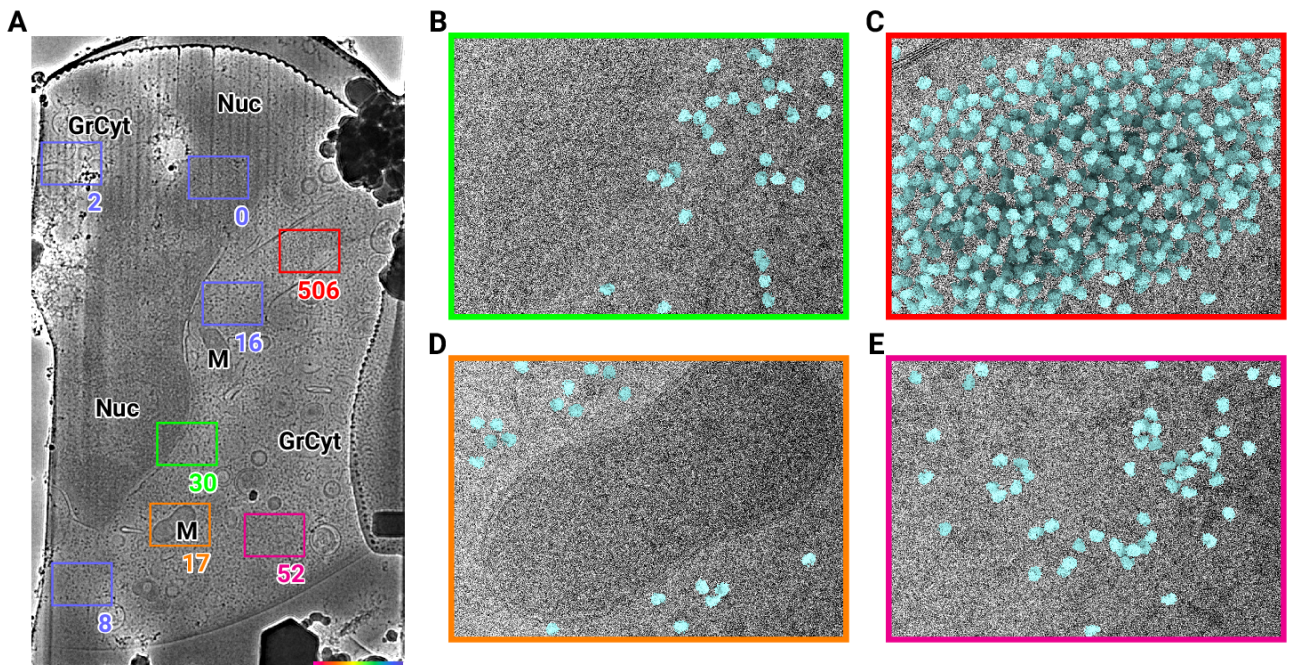


Figure 2: 2D template matching of the large subunit of the ribosome in fib-milled neutrophil-like cells (A) Overview image of the lamella. Major cellular regions are labeled, as Nucleus (Nuc), Mitochondria (M), and granular cytoplasm (GrCyt). FOVs where high-magnification images for template matching were acquired are indicated as boxes with the number of detected targets indicated on the bottom right. FOVs displayed in Panels B-E are color-coded. Scalebar corresponds to 1 m. (B-E) FOVs with projection of detected LSUs shown in cyan. (B) Perinuclear region, the only detected targets are in the cytoplasmic half. (C) Cytoplasmic region with high density of ribosomes (D) Mitochondrion, as expected there are only detected LSUs in the cytoplasmic region (E) Cytoplasm, with low density of ribosomes.

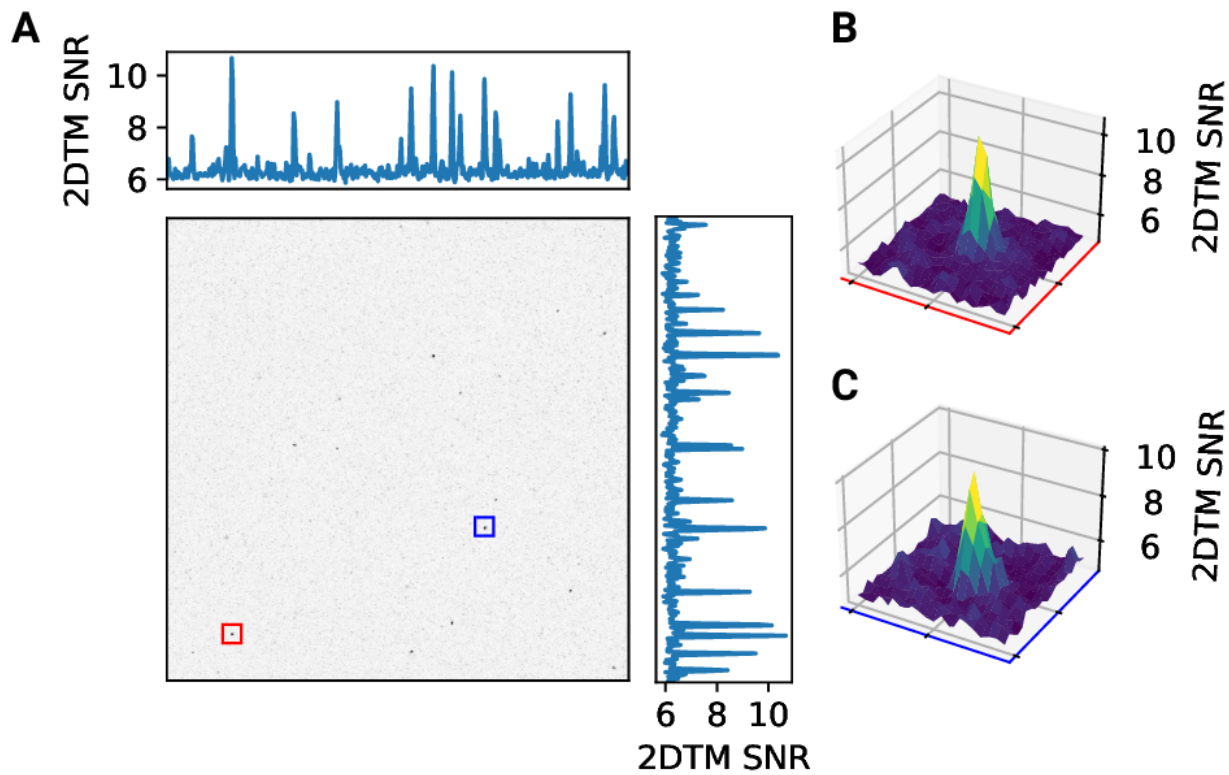


Figure 2 - figure supplement 1: 2D template matching of the large subunit of the ribosome in fib-milled neutrophil-like cells (A) Maximum intensity projection (MIP) cross-correlation map of micrograph shown in Figure 2 (B+C) 3D plot of MIP regions indicated by color boxes in Panel A

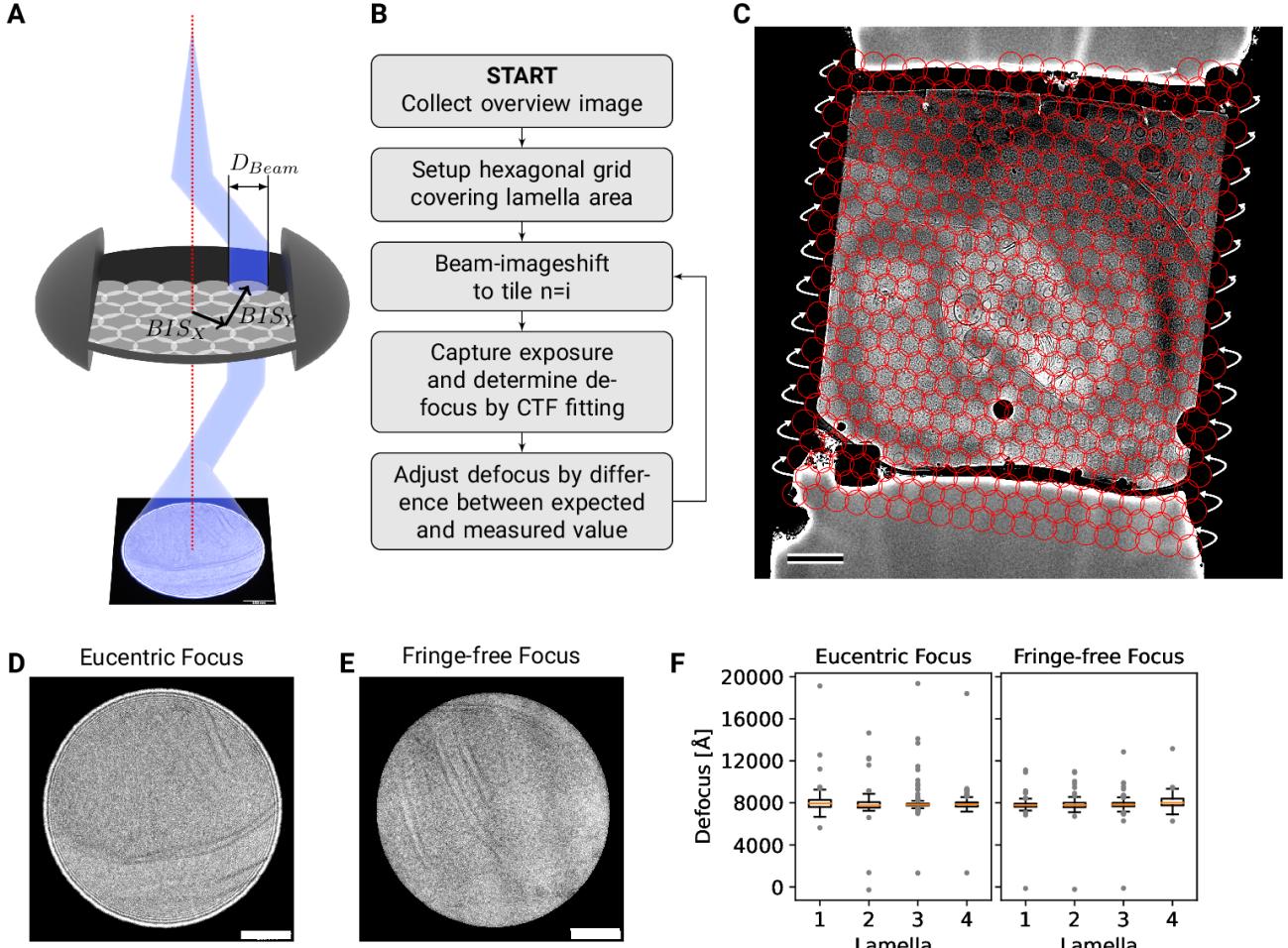


Figure 3: DeCo-LACE approach (A) Graphic demonstrating the data-collection strategy for DeCo-LACE. The electron beam is condensed to a diameter  $D_{Beam}$  that allows captured of the whole illuminated area on the camera. Beam-image shift along X and Y ( $BIS_X, BIS_Y$ ) is used to scan the whole lamella (B) Diagram of the collection algorithm (C) Example overview image of a lamella with the designated acquisition positions and the used beam diameter indicated with red circles. Scalebar corresponds to 1 m. (D+E) Representative micrographs taken with a condensed beam at eucentric focus (D) or fringe-free focus (E). Scalebar corresponds to 100 nm. (F) Boxplot of defocus measured by ctffind of micrographs taken by the DeCo-Lace approach on four lamellae images at eucentric focus and four lamellae imaged with fringe-free focus.

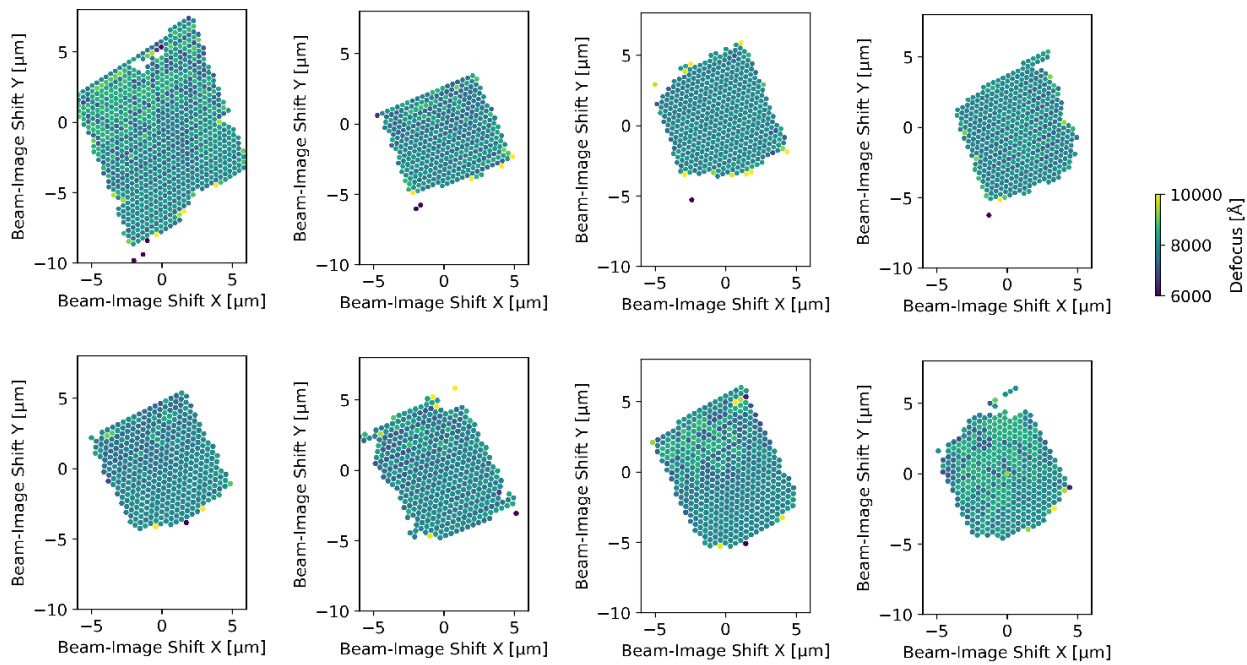
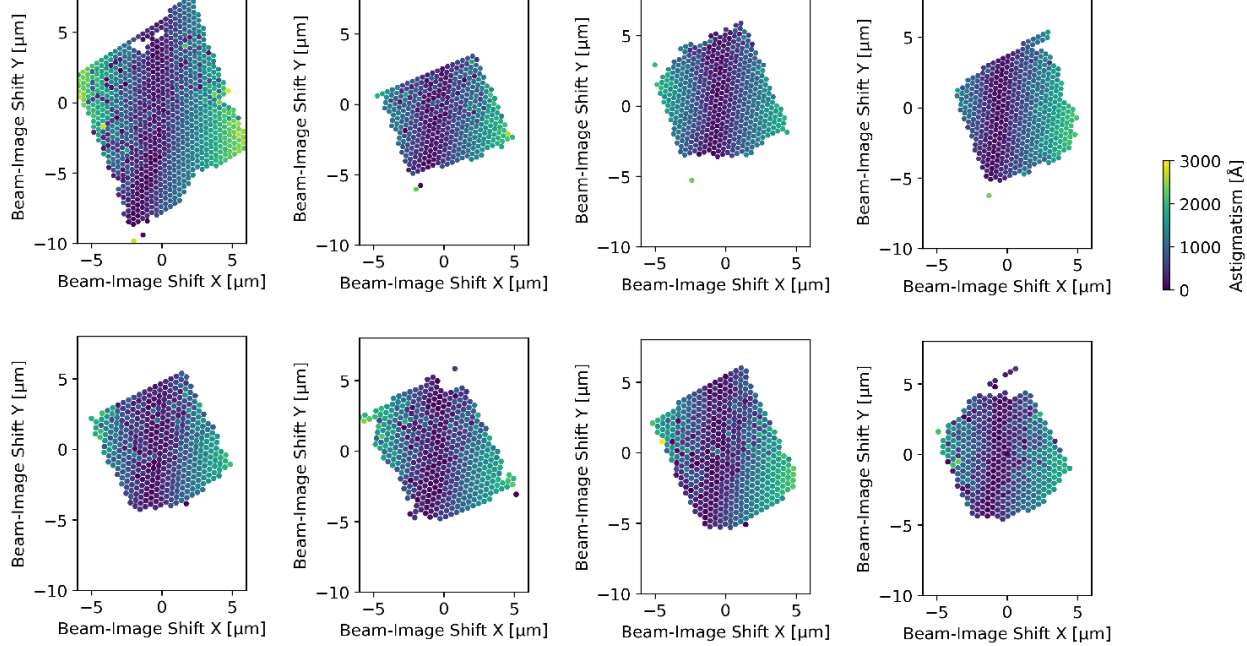
**A****B**

Figure 3 - figure supplement 1: Defocus estimation of individual tiles of DeCo-Lace montages (A) Defocus values of individual micrographs taken using the DeCo-Lace approach plotted as a function of the beam image-shift values. (B) Defocus astigmatism of individual micrographs taken using the DeCo-Lace approach plotted as a function of the beam image-shift values.

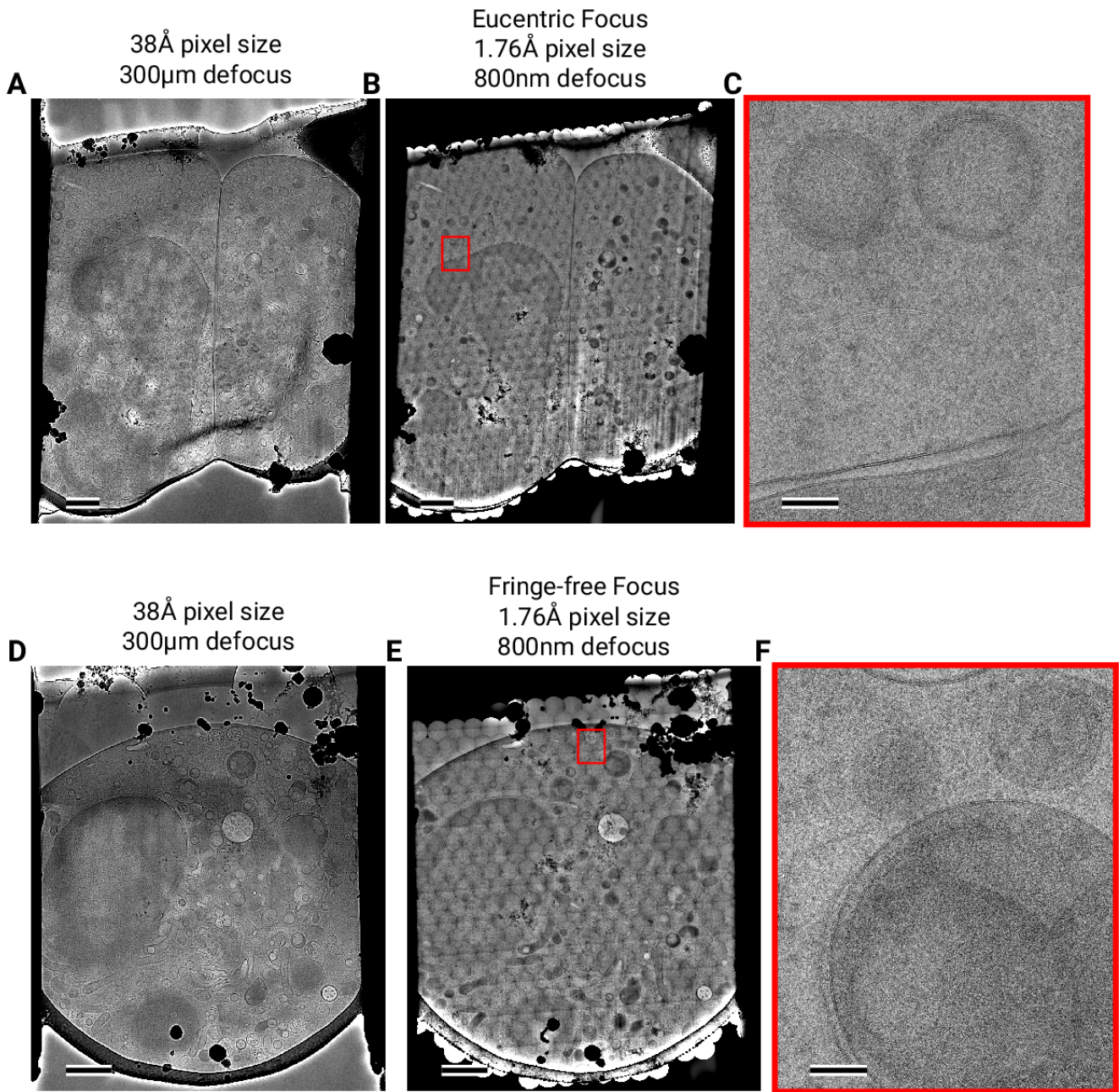


Figure 4: Assembling DeCo-LACE exposures into montages (A) Overview image of Lamella<sub>EUC</sub> 1 taken at low magnification. Scalebar corresponds to 1 m. (B) Overview of Lamella<sub>EUC</sub> 1 created by montaging high magnification images taken with the DeCo-Lace approach. Scalebar corresponds to 1 m. (C) Zoom-in into red box in panel B. Slight beam-fringe artifacts are visible. Scalebar corresponds to 100 nm. (D) Overview image of Lamella<sub>FFF</sub> 4 taken at low magnification. Scalebar corresponds to 1 m. (E) Overview of Lamella<sub>FFF</sub> 4 created by montaging high magnification images taken with the DeCo-Lace approach. Scalebar corresponds to 1 m. (F) Zoom-in into red box in panel E. No beam-fringe artifacts are visible. Scalebar corresponds to 100 nm.

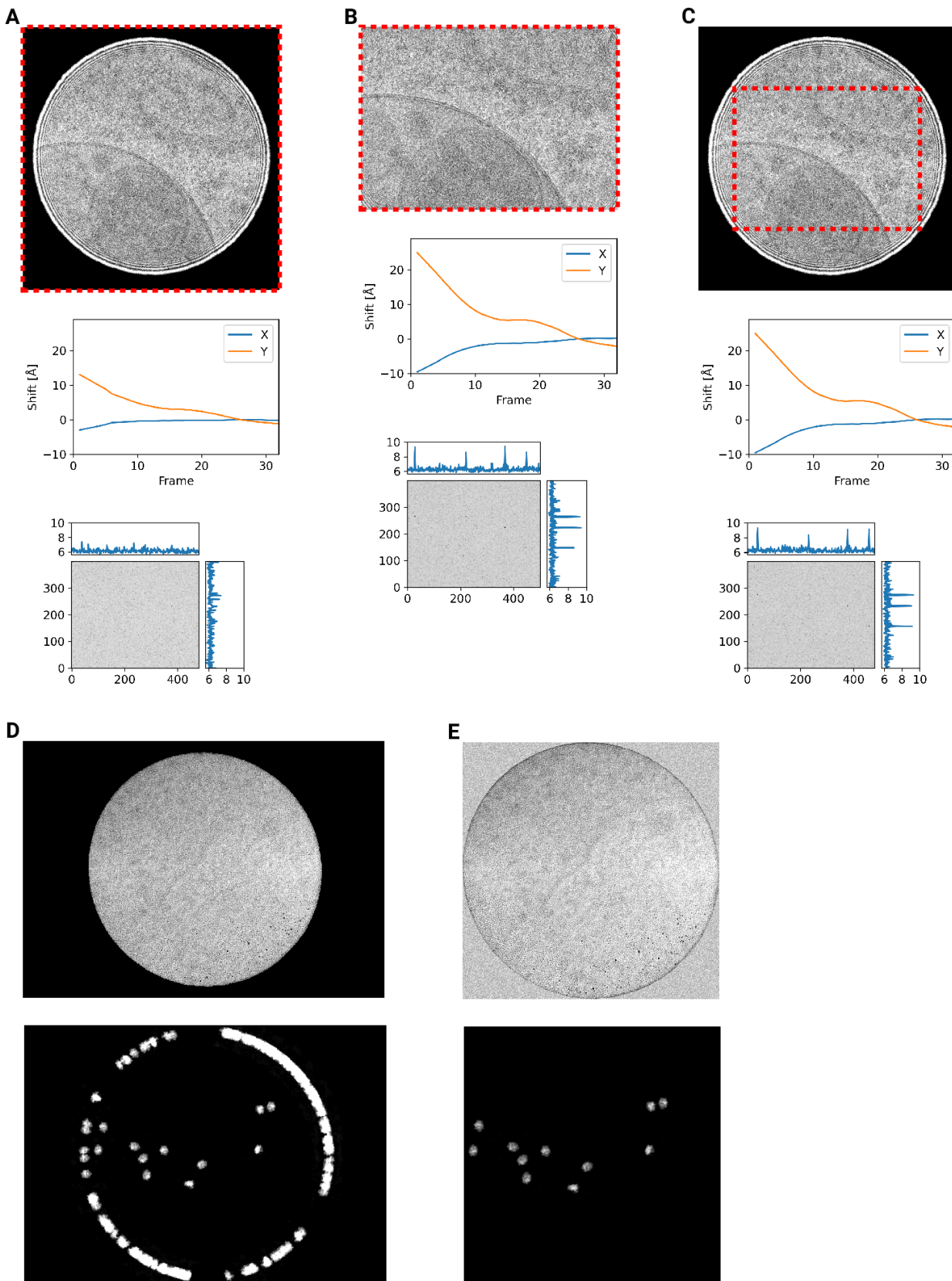


Figure 4 - figure supplement 1: Motion correction of movies with condensed beams. At the top of each panel is an average of the movie that was motion-corrected with a red dashed box indicating the region that was used to estimate shifts. Below is a graph indicating the estimated shifts of the individual frames of the movie. Below this is the MIP of 2DTM using the large subunit of the mouse ribosome. (A) Motion correction of the whole movie (B) Motion correction of a cropped region of the movie that eliminates the beam edges (C) Motion correction of the whole movie, using only the central region to estimate the shifts

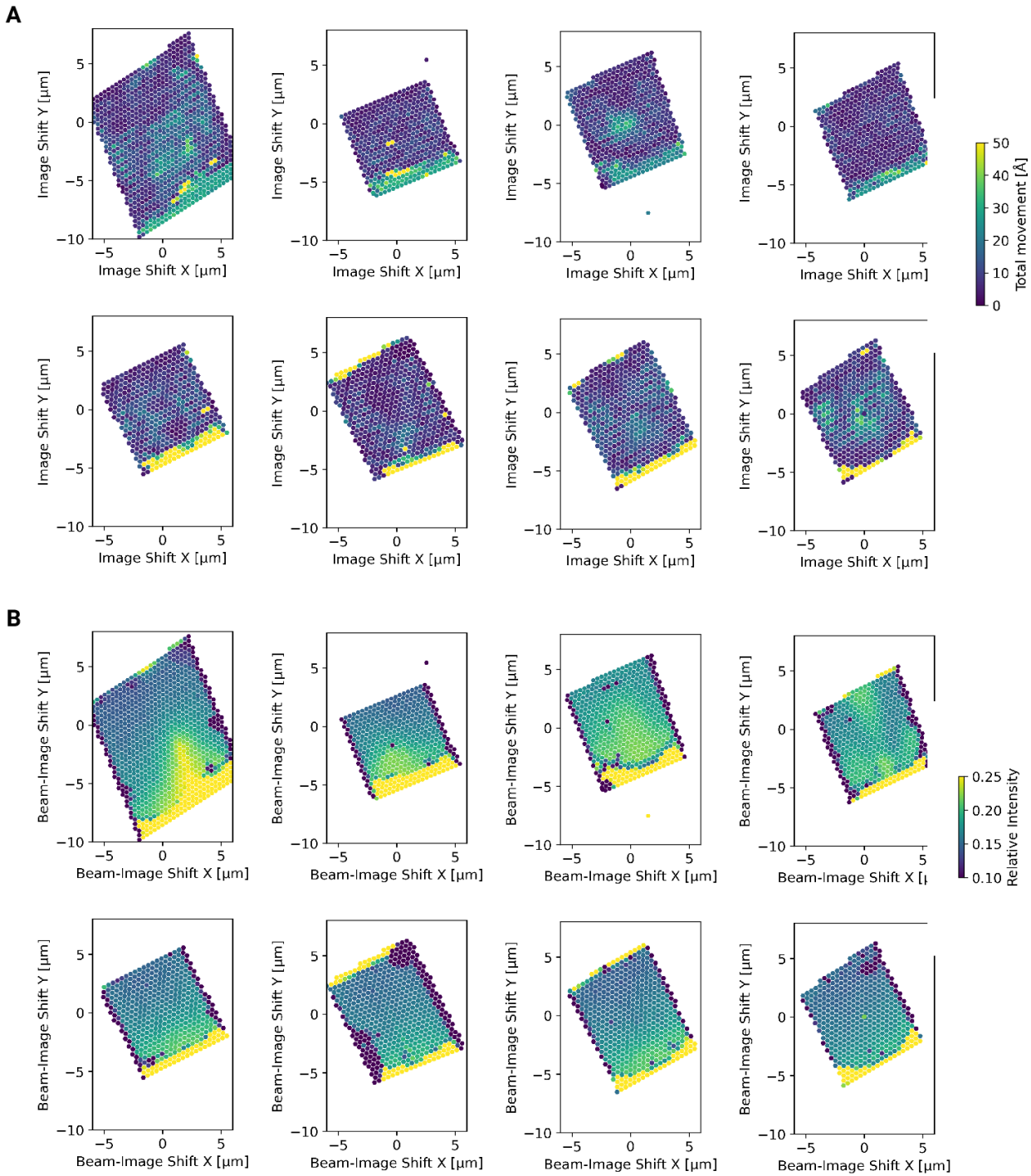


Figure 4 - figure supplement 2: Motion correction of individual tiles imaged using the DeCo-LACE approach (A) Total estimated motion of individual micrographs taken using the DeCo-Lace approach plotted as a function of the beam image-shift values. (B) Electron intensity of individual micrographs taken using the DeCo-Lace approach plotted as a function of the beam image-shift values.

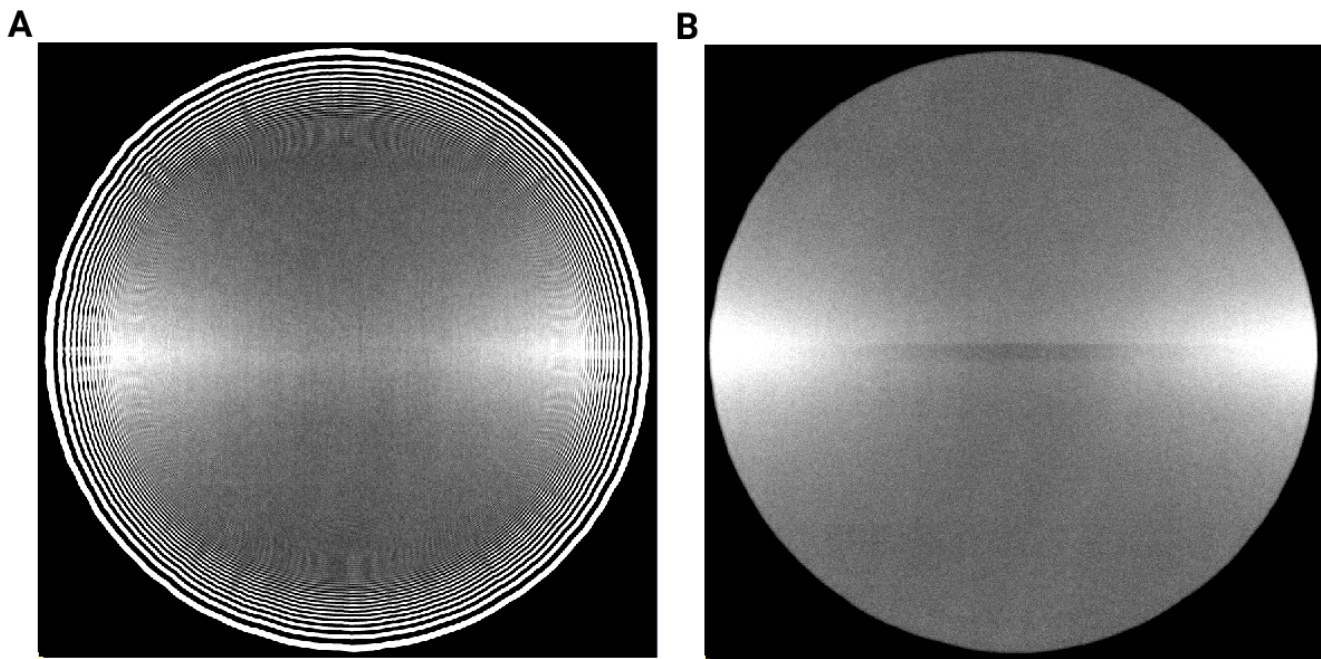


Figure 4 - figure supplement 3: Averages of micrographs taken with a condensed beam over vacuum using a Gatan K3 detector. Contrast and Brightness have been adjusted to highlight uneven dose response. (A) Eucentric Focus (B) Fringe-free Focus

356 4. **Electron microscopy of frozen hydrated sections of vitreous ice and vitrified biological samples**  
 AW McDowall, J-J Chang, R Freeman, J Lepault, CA Walter, J Dubochet  
*Journal of Microscopy* (1983-07) <https://doi.org/bdnzmv> DOI: 10.1111/j.1365-2818.1983.tb04225.x ·  
 PMID: 6350598

357  
 358 5. **Opening windows into the cell: focused-ion-beam milling for cryo-electron tomography**  
 Elizabeth Villa, Miroslava Schaffer, Jürgen M Plitzko, Wolfgang Baumeister  
*Current Opinion in Structural Biology* (2013-10) <https://doi.org/f537jp> DOI: 10.1016/j.sbi.2013.08.006 ·  
 PMID: 24090931

359  
 360 6. **Electron tomography of cells** Lu Gan, Grant J Jensen  
*Quarterly Reviews of Biophysics* (2011-11-15) <https://doi.org/czj9hr> DOI: 10.1017/s0033583511000102 ·  
 PMID: 22082691

361  
 362 7. **Single-protein detection in crowded molecular environments in cryo-EM images** JPeter Rick-  
 gauer, Nikolaus Grigorieff, Winfried Denk  
*eLife* (2017-05-03) <https://doi.org/gnq4q4> DOI: 10.7554/elife.25648 · PMID: 28467302 · PMCID:  
 PMC5453696

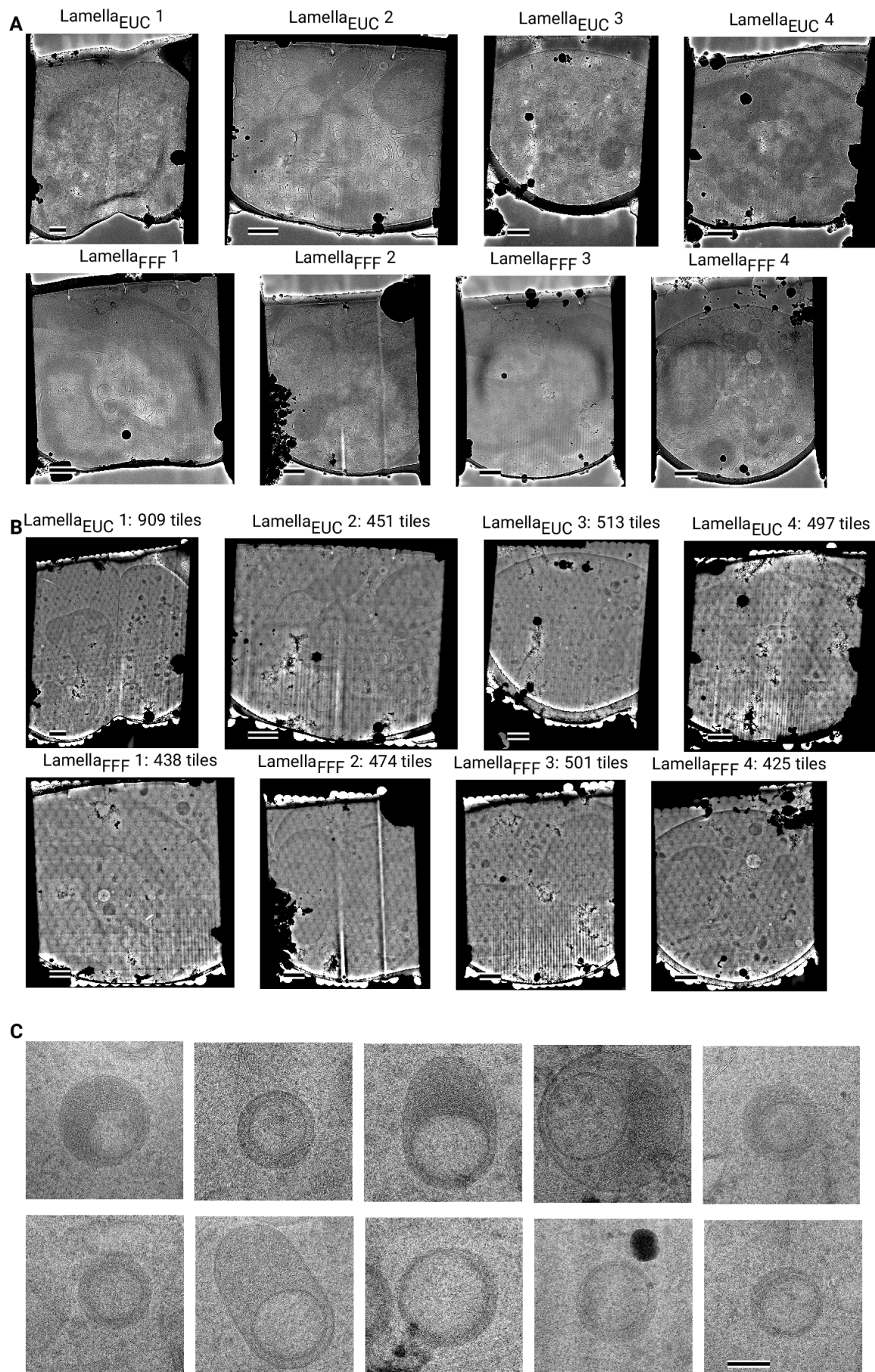


Figure 4 - figure supplement 4: Overview images of lamellae imaged using the DeCo-LACE approach taken at low-magnification (A) Overviews taken at low magnification.<sup>22</sup> Scalebar corresponds to 1 m. (B) Overviews assembled using the DeCo-LACE approach. Scalebar corresponds to 1 m. (C) Representative examples of a class of granules containing a putatively cytosolic inclusion. Scalebar corresponds to 100 nm.

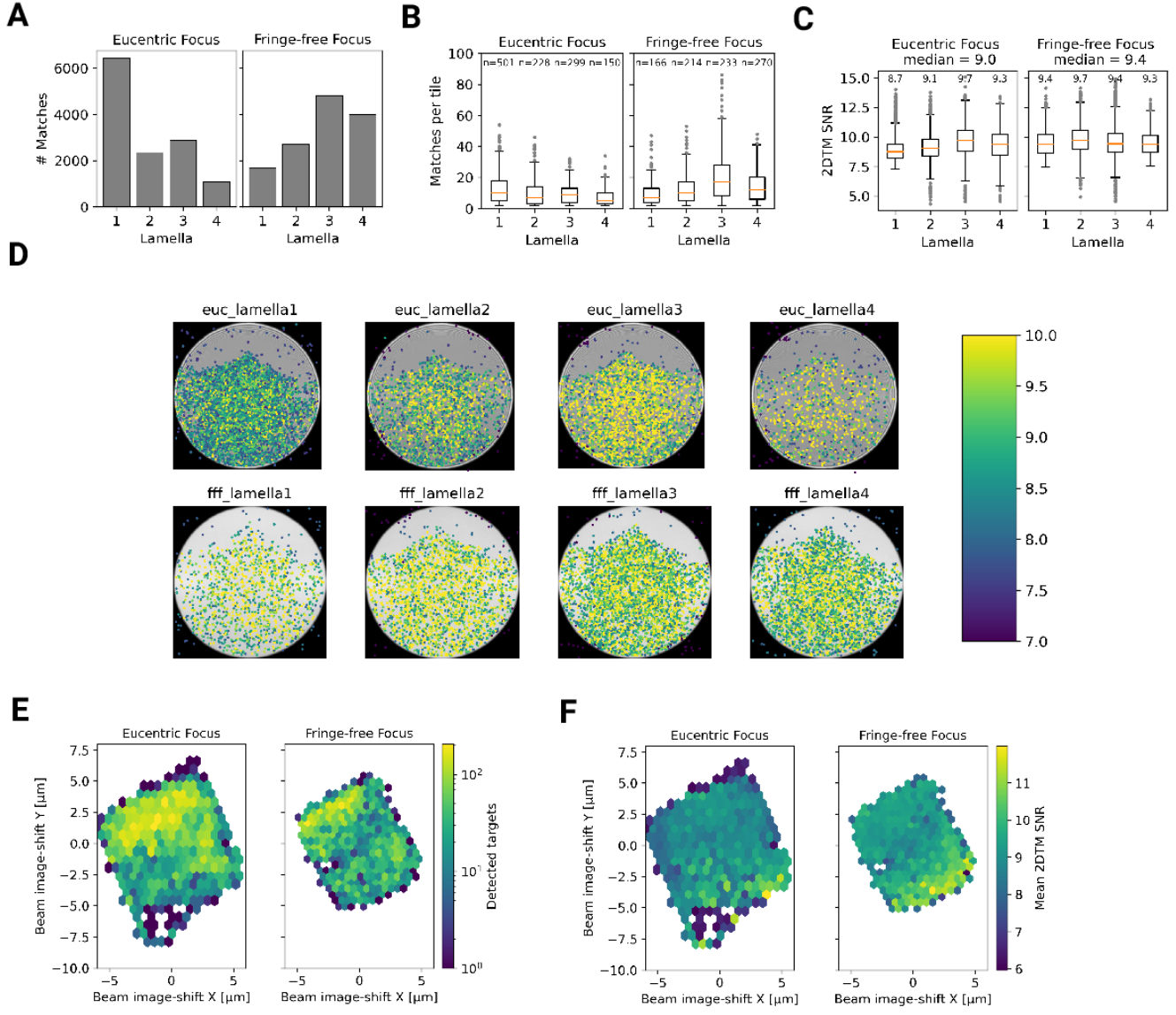


Figure 5: Statistics of 2DTM on lamella imaged using DeCo-LACE (A) Number of detected targets in each lamella (B) Distribution of targets per tile in each lamella. Only tiles with two or more detected targets were included (C) Distribution of SNRs in each lamella (D) For each lamella an average of all tiles is shown. Overlaid is a scatterplot of all detected targets in these tiles according to their in-tile coordinates. Scatterplot is colored according to the 2DTM SNR. There are no detected targets in the top circle-circle intersection due to radiation damage from previous exposures. (E) 2D histogram of number of detected targets as a function of beam-image shift (F) Mean 2DTM SNR as a function of beam-image shift

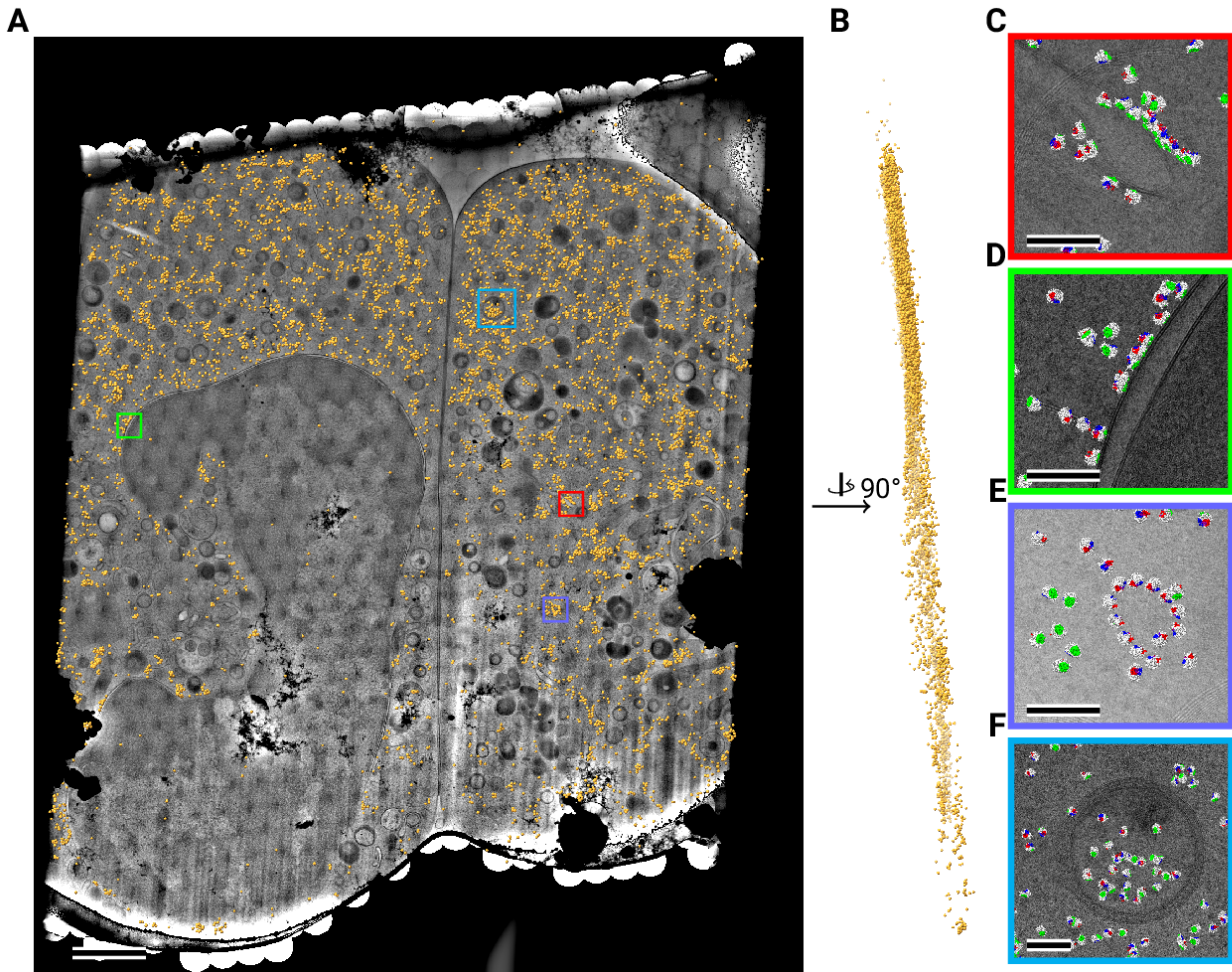


Figure 6: Template matching in lamella imaged using the DeCo-Lace approach at eucentric focus (A) Montage of Lamella<sub>EUC</sub> 1 overlaid with detected targets according to their montage coordinates colored in orange. Scalebar corresponds to 1 m. (B) Side view of detected targets in the lamella, such that the direction of the electron beam is horizontal. (C-F) Magnified area of panel A showing rough ER with associated ribosomes(C), outer nuclear membrane with associated ribosomes (D), ribosomes arranged in a circular fashion(E), ribosomes enclosed in a less electron dense inclusion in a granule(F). Ribosomes are colored in white with the surface of the peptide exit tunnel colored in green and the A, P, and E sites colored in blue, purple, and red, respectively. Scalebar corresponds to 100 nm.

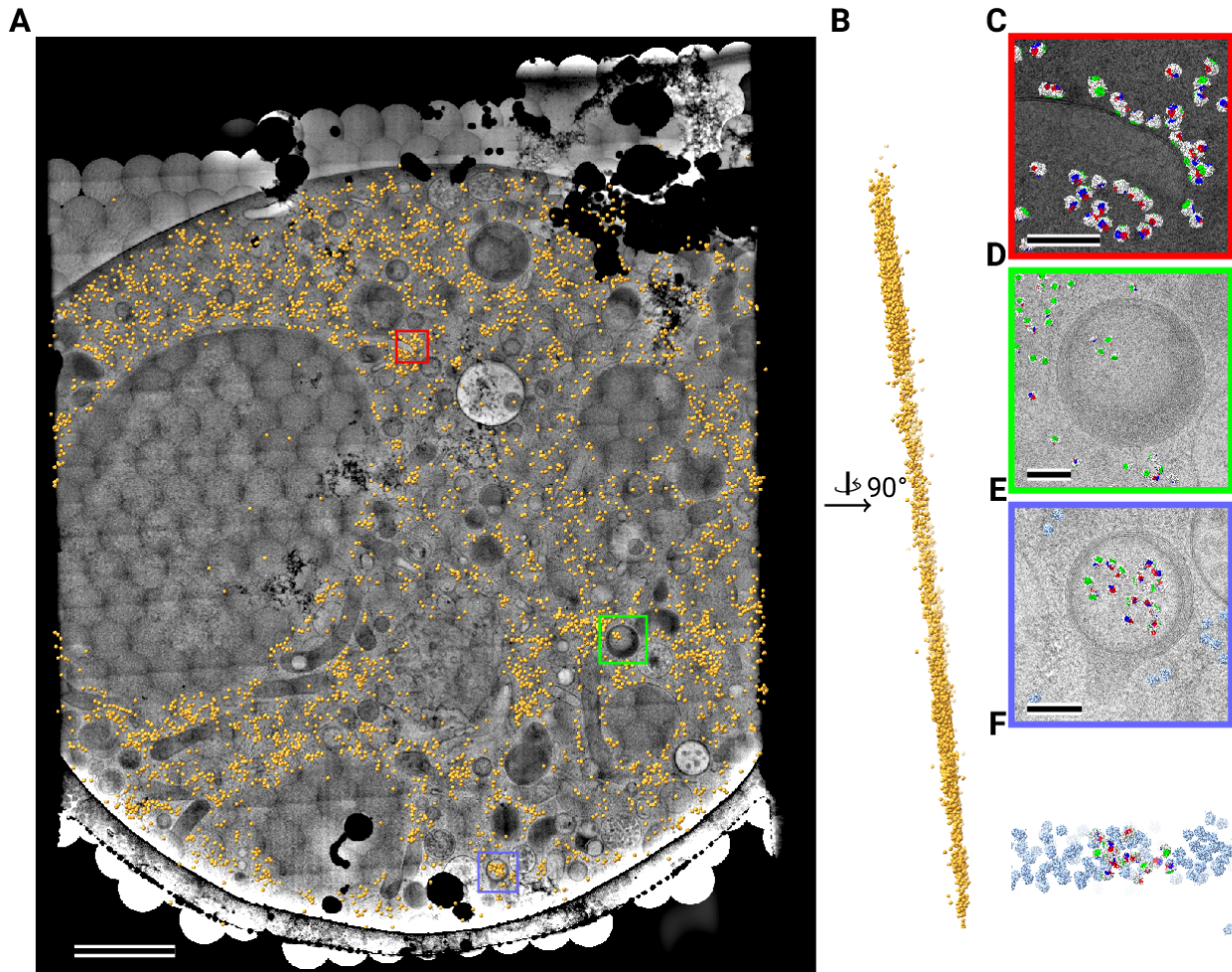


Figure 7: Template matching in lamella imaged using the DeCo-Lace approach at fringe-free focus (A) Montage of Lamella<sub>FFF</sub> 4 overlaid with detected targets according to their montage coordinates colored in orange. Scalebar corresponds to 1 m. (B) Side view of detected targets in the lamella, such that the direction of the electron beam is horizontal. (C-E) Magnified area of panel A showing rough ER with associated ribosomes(C) and ribosomes enclosed in a less electron dense inclusion in a granule(D,E). (F) Side view of panel E. Ribosomes are colored in white with the surface of the peptide exit tunnel colored in green and the A, P, and E sites colored in blue, purple, and red, respectively. Scalebar corresponds to 100 nm.

363

- 364 8. **Label-free single-instance protein detection in vitrified cells** JPeter Rickgauer, Heejun Choi,  
Jennifer Lippincott-Schwartz, Winfried Denk  
*Cold Spring Harbor Laboratory* (2020-04-24) <https://doi.org/gpbjfd> DOI: 10.1101/2020.04.22.053868

365

- 366 9. **Locating macromolecular assemblies in cells by 2D template matching with cisTEM** Bronwyn  
A Lucas, Benjamin A Himes, Liang Xue, Timothy Grant, Julia Mahamid, Nikolaus Grigorieff  
*eLife* (2021-06-11) <https://doi.org/gkkc49> DOI: 10.7554/elife.68946 · PMID: 34114559 · PMCID:  
PMC8219381

367

- 368 10. **Inhibition of Dihydroorotate Dehydrogenase Overcomes Differentiation Blockade in Acute  
Myeloid Leukemia** David B Sykes, Youmna S Kfouri, François E Mercier, Mathias J Wawer, Jason M  
Law, Mark K Haynes, Timothy A Lewis, Amir Schajnovitz, Esha Jain, Dongjun Lee, ... David T Scadden  
*Cell* (2016-09) <https://doi.org/f3r5jr> DOI: 10.1016/j.cell.2016.08.057 · PMID: 27641501 · PMCID:  
PMC7360335

369

- 370 11. **Hallmarks of ribosomopathies** Kim R Kampen, Sergey O Sulima, Stijn Vereecke, Kim De Keersmaecker  
*Nucleic Acids Research* (2019-07-27) <https://doi.org/gpbjfm> DOI: 10.1093/nar/gkz637 · PMID: 31350888  
· PMCID: PMC7026650

371

- 372 12. **Diagnostic and prognostic implications of ribosomal protein transcript expression patterns in  
human cancers** James M Dolezal, Arie P Dash, Edward V Prochownik  
*BMC Cancer* (2018-03-12) <https://doi.org/gc87j9> DOI: 10.1186/s12885-018-4178-z · PMID: 29530001 ·  
PMCID: PMC5848553

373

- 374 13. **Automated electron microscope tomography using robust prediction of specimen movements**  
David N Mastronarde  
*Journal of Structural Biology* (2005-10) <https://doi.org/ff7gzx> DOI: 10.1016/j.jsb.2005.07.007 · PMID:  
16182563

375

- 376 14. **cisTEM, user-friendly software for single-particle image processing** Timothy Grant, Alexis Rohou,  
Nikolaus Grigorieff  
*eLife* (2018-03-07) <https://doi.org/gf5cq7> DOI: 10.7554/elife.35383 · PMID: 29513216 · PMCID:  
PMC5854467
- 377
- 378 15. **Measuring the optimal exposure for single particle cryo-EM using a 2.6 Å reconstruction of  
rotavirus VP6** Timothy Grant, Nikolaus Grigorieff  
*eLife* (2015-05-29) <https://doi.org/gf5cm7> DOI: 10.7554/elife.06980 · PMID: 26023829 · PMCID:  
PMC4471936
- 379
- 380 16. **CTFFIND4: Fast and accurate defocus estimation from electron micrographs** Alexis Rohou,  
Nikolaus Grigorieff  
*Journal of Structural Biology* (2015-11) <https://doi.org/f7xzgv> DOI: 10.1016/j.jsb.2015.08.008 · PMID:  
26278980 · PMCID: PMC6760662
- 381
- 382 17. **Cryo-TEM simulations of amorphous radiation-sensitive samples using multislice wave propa-  
gation** Benjamin Himes, Nikolaus Grigorieff  
*IUCrJ* (2021-09-30) <https://doi.org/gpzs9r> DOI: 10.1107/s2052252521008538 · PMID: 34804546 · PMCID:  
PMC8562658
- 383
- 384 18. **scikit-image: image processing in Python** Stéfan van der Walt, Johannes L Schönberger, Juan  
Nunez-Iglesias, François Boulogne, Joshua D Warner, Neil Yager, Emmanuelle Gouillart, Tony Yu  
*PeerJ* (2014-06-19) <https://doi.org/gftp3s> DOI: 10.7717/peerj.453 · PMID: 25024921 · PMCID:  
PMC4081273
- 385
- 386 19. **SciPy 1.0: fundamental algorithms for scientific computing in Python** Pauli Virtanen, Ralf  
Gommers, Travis E Oliphant, Matt Haberland, Tyler Reddy, David Cournapeau, Evgeni Burovski, Pearu  
Peterson, Warren Weckesser, Jonathan Bright, ...  
*Nature Methods* (2020-02-03) <https://doi.org/ggj45f> DOI: 10.1038/s41592-019-0686-2 · PMID: 32015543 ·  
PMCID: PMC7056644

387

- 388 20. <scp>UCSF ChimeraX</scp> : Structure visualization for researchers, educators, and  
developers Eric F Pettersen, Thomas D Goddard, Conrad C Huang, Elaine C Meng, Gregory S Couch,  
Tristan I Croll, John H Morris, Thomas E Ferrin  
*Protein Science* (2020-10-22) <https://doi.org/ghr6mn> DOI: 10.1002/pro.3943 · PMID: 32881101 · PMCID:  
PMC7737788
- 389
- 390 21. **Protein Synthesis in the Developing Neocortex at Near-Atomic Resolution Reveals Ebp1-Mediated Neuronal Proteostasis at the 60S Tunnel Exit** Matthew L Kraushar, Ferdinand Krupp, Dermot Harnett, Paul Turko, Mateusz C Ambrozkiewicz, Thiemo Sprink, Koshi Imami, Manuel Günnigmann, Ulrike Zinnall, Carlos H Vieira-Vieira, ... Christian MT Spahn  
*Molecular Cell* (2021-01) <https://doi.org/gh7d72> DOI: 10.1016/j.molcel.2020.11.037 · PMID: 33357414 ·  
PMCID: PMC8163098
- 391
- 392 22. **High-quality, high-throughput cryo-electron microscopy data collection via beam tilt and astigmatism-free beam-image shift** Chunling Wu, Xiaojun Huang, Jing Cheng, Dongjie Zhu, Xinzhen Zhang  
*Journal of Structural Biology* (2019-12) <https://doi.org/gp2nq9> DOI: 10.1016/j.jsb.2019.09.013 · PMID:  
31562921
- 393
- 394 23. **THE DEVELOPMENT OF NEUTROPHILIC POLYMORPHONUCLEAR LEUKOCYTES IN HUMAN BONE MARROW** Dorothy Ford Bainton, Joan L Ulyot, Marilyn G Farquhar  
*Journal of Experimental Medicine* (1971-10-01) <https://doi.org/chkbcm> DOI: 10.1084/jem.134.4.907 ·  
PMID: 4106490 · PMCID: PMC2138991
- 395
- 396 24. **Routine determination of ice thickness for cryo-EM grids** William J Rice, Anchi Cheng, Alex J Noble, Edward T Eng, Laura Y Kim, Bridget Carragher, Clinton S Potter  
*Journal of Structural Biology* (2018-10) <https://doi.org/gfbpj2> DOI: 10.1016/j.jsb.2018.06.007 · PMID:  
29981485 · PMCID: PMC6119488

- 398 25. **Optimized cryo-focused ion beam sample preparation aimed at *in situ* structural studies of membrane proteins** Miroslava Schaffer, Julia Mahamid, Benjamin D Engel, Tim Laugks, Wolfgang Baumeister, Jürgen M Plitzko  
*Journal of Structural Biology* (2017-02) <https://doi.org/f9qfr6> DOI: 10.1016/j.jsb.2016.07.010 · PMID: 27444390
- 399
- 400 26. **Circularization of mRNA by eukaryotic translation initiation factors.** SE Wells, PE Hillner, RD Vale, AB Sachs  
*Molecular cell* (1998-07) <https://www.ncbi.nlm.nih.gov/pubmed/9702200> DOI: 10.1016/s1097-2765(00)80122-7 · PMID: 9702200
- 401
- 402 27. **Montage electron tomography of vitrified specimens** Ariana Peck, Stephen D Carter, Huanghao Mai, Songye Chen, Alister Burt, Grant J Jensen  
*Journal of Structural Biology* (2022-06) <https://doi.org/gp4qrs> DOI: 10.1016/j.jsb.2022.107860 · PMID: 35487464
- 403
- 404 28. **Correlative cryogenic montage electron tomography for comprehensive *in-situ* whole-cell structural studies** Jie E Yang, Matthew R Larson, Bryan S Sibert, Joseph Y Kim, Daniel Parrell, Juan C Sanchez, Victoria Pappas, Anil Kumar, Kai Cai, Keith Thompson, Elizabeth R Wright  
*Cold Spring Harbor Laboratory* (2022-01-02) <https://doi.org/gp4qrw> DOI: 10.1101/2021.12.31.474669
- 405
- 406 29. **Beam image-shift accelerated data acquisition for near-atomic resolution single-particle cryo-electron tomography** Jonathan Bouvette, Hsuan-Fu Liu, Xiaochen Du, Ye Zhou, Andrew P Sikkema, Juliana da Fonseca Rezende e Mello, Bradley P Klemm, Rick Huang, Roel M Schaaper, Mario J Borgnia, Alberto Bartesaghi  
*Nature Communications* (2021-03-30) <https://doi.org/gjphkb> DOI: 10.1038/s41467-021-22251-8 · PMID: 33785757 · PMCID: PMC8009872
- 407
- 408 30. **Parallel cryo electron tomography on < i > *in situ* </ i > lamellae** Fabian Eisenstein, Haruaki Yanagisawa, Hiroka Kashihara, Masahide Kikkawa, Sachiko Tsukita, Radostin Danev  
*Cold Spring Harbor Laboratory* (2022-04-08) <https://doi.org/gp4qrw> DOI: 10.1101/2022.04.07.487557

409

- 410 31. **Waffle Method: A general and flexible approach for improving throughput in FIB-milling**  
Kotaro Kelley, Ashleigh M Raczkowski, Oleg Klykov, Pattana Jaroenlak, Daija Bobe, Mykhailo Kopylov,  
Edward T Eng, Gira Bhabha, Clinton S Potter, Bridget Carragher, Alex J Noble  
*Nature Communications* (2022-04-06) <https://doi.org/gp4qrt> DOI: 10.1038/s41467-022-29501-3 · PMID:  
35387991 · PMCID: PMC8987090
- 411
- 412 32. **< i > In situ < /i > single particle classification reveals distinct 60S maturation intermediates in**  
**cells** Bronwyn A Lucas, Kexin Zhang, Sarah Loerch, Nikolaus Grigorieff  
*Cold Spring Harbor Laboratory* (2022-04-10) <https://doi.org/gp4qrz> DOI: 10.1101/2022.04.10.487797
- 413
- 414 33. **High-resolution cryo-EM using beam-image shift at 200 keV** Jennifer N Cash, Sarah Kearns, Yilai  
Li, Michael A Cianfrocco  
*IUCrJ* (2020-10-29) <https://doi.org/gjwcfq> DOI: 10.1107/s2052252520013482 · PMID: 33209328 · PMCID:  
PMC7642776
- 415
- 416 34. **Shedding light on the cell biology of extracellular vesicles** Guillaume van Niel, Gisela D'Angelo,  
Graça Raposo  
*Nature Reviews Molecular Cell Biology* (2018-01-17) <https://doi.org/gct4df> DOI: 10.1038/nrm.2017.125 ·  
PMID: 29339798
- 417
- 418 35. **Exosome-mediated transfer of mRNAs and microRNAs is a novel mechanism of genetic**  
**exchange between cells** Hadi Valadi, Karin Ekström, Apostolos Bossios, Margareta Sjöstrand, James J  
Lee, Jan O Lötvall  
*Nature Cell Biology* (2007-05-07) <https://doi.org/d5df4s> DOI: 10.1038/ncb1596 · PMID: 17486113